



Structural and Dynamical Analysis of the Quiescent Molecular Ridge in the Large Magellanic Cloud

Molly K. Finn¹ , Remy Indebetouw^{1,2} , Kelsey E. Johnson¹ , Allison H. Costa² , C.-H. Rosie Chen³ , Akiko Kawamura⁴ , Toshikazu Onishi⁵ , Jürgen Ott^{6,7} , Marta Sewilo^{8,9,10} , Kazuki Tokuda^{4,11} , Tony Wong¹² , and Sarolta Zahorecz^{4,5}

¹ Department of Astronomy, University of Virginia, Charlottesville, VA 22904, USA

² National Radio Astronomy Observatory, 520 Edgemont Road, Charlottesville, VA 22903, USA

³ Max-Planck-Institut für Radioastronomie, Auf dem Hügel 69, D-53121 Bonn, Germany

⁴ National Astronomical Observatory of Japan, National Institutes of Natural Sciences, 2-21-1 Osawa, Mitaka, Tokyo 181-8588, Japan

⁵ Department of Physics, Graduate School of Science, Osaka Metropolitan University, 1-1 Gakuen-cho, Naka-ku, Sakai, Osaka 599-8531, Japan

⁶ National Radio Astronomy Observatory, P.O. Box O, Socorro, NM 87801, USA

⁷ Physics Department, New Mexico Institute of Mining and Technology, 801 Leroy Pl., Socorro, NM 87801, USA

⁸ Exoplanets and Stellar Astrophysics Laboratory, NASA Goddard Space Flight Center, Greenbelt, MD 20771, USA

⁹ Department of Astronomy, University of Maryland, College Park, MD 20742, USA

¹⁰ Center for Research and Exploration in Space Science and Technology, NASA Goddard Space Flight Center, Greenbelt, MD 20771, USA

¹¹ Department of Earth and Planetary Sciences, Faculty of Sciences, Kyushu University, Nishi-ku, Fukuoka 819-0395, Japan

¹² Astronomy Department, University of Illinois, 1002 W. Green Street, Urbana, IL 61801, USA; mf4yu@virginia.edu

Received 2022 April 6; revised 2022 June 17; accepted 2022 June 19; published 2022 July 21

Abstract

We present a comparison of low- J ^{13}CO and CS observations of four different regions in the LMC—the quiescent Molecular Ridge, 30 Doradus, N159, and N113, all at a resolution of ~ 3 pc. The regions 30 Dor, N159, and N113 are actively forming massive stars, while the Molecular Ridge is forming almost no massive stars, despite its large reservoir of molecular gas and proximity to N159 and 30 Dor. We segment the emission from each region into hierarchical structures using dendrograms and analyze the sizes, masses, and line widths of these structures. We find that the Ridge has significantly lower kinetic energy at a given size scale and also lower surface densities than the other regions, resulting in higher virial parameters. This suggests that the Ridge is not forming massive stars as actively as the other regions because it has less dense gas and not because collapse is suppressed by excess kinetic energy. We also find that these physical conditions and energy balance vary significantly within the Ridge and that this variation appears only weakly correlated with distance from sites of massive-star formation such as R136 in 30 Dor, which is ~ 1 kpc away. These variations also show only a weak correlation with local star formation activity within the clouds.

Unified Astronomy Thesaurus concepts: [Interstellar medium \(847\)](#); [Molecular clouds \(847\)](#); [Large Magellanic Cloud \(903\)](#); [Star formation \(1569\)](#); [Millimeter astronomy \(1061\)](#)

1. Introduction

Star formation is a crucial component of our understanding of galactic environments. As we study galaxies at a wide variety of distance scales and size scales, we look for easily observable tracers of star formation and molecular gas behavior, such as the Schmidt–Kennicutt law relating molecular gas surface density and galactic star formation rate (Kennicutt 1998). These relations have had success at predicting star formation rates in many environments, but we also know of cases where those relations do not hold. For example, the Central Molecular Zone of our own Galaxy is forming stars an order of magnitude slower than we would expect for a region with so much molecular gas available (Longmore et al. 2013). It is clear that while these relations hold well on galactic scales, the physical conditions that give rise to such relations are not constant across different environments within a galaxy.

The Large Magellanic Cloud (LMC) is an excellent laboratory in which to study the variations in galactic environments. At a distance of 50 kpc (Pietrzyński et al.

2013), it is close enough that we can resolve individual molecular clouds, while its low inclination angle ($\sim 34^\circ$; van der Marel & Kallivayalil 2014) allows us a clear view of the contents of the galaxy with little line-of-sight or distance confusion. It also hosts a wide variety of star-forming environments, making comparisons between them relatively straightforward since they share a common distance, metallicity ($Z \sim 0.5 Z_\odot$; Rolleston et al. 2002), and galactic environment. In this paper, we focus our analysis on the quiescent Molecular Ridge, 30 Doradus (30 Dor), N159, and N113 to span the extremes of star formation in the LMC.

The Molecular Ridge (also referred to throughout this work as “the Ridge”) is a ~ 2 kpc long structure in the LMC and contains nearly 30% of all the CO-bright molecular gas mass in the galaxy (Cohen et al. 1988; Fukui et al. 2008; Mizuno et al. 2001; see Figure 1). Despite this large quantity of molecular gas, the southern part of the Ridge is forming very few massive stars, based on low $\text{H}\alpha$ emission and a lack of optically identified young massive clusters (Davies et al. 1976; Bica et al. 1996; Yamaguchi et al. 2001).

Indebetouw et al. (2008) found that the Schmidt–Kennicutt law (Kennicutt 1998) predicts that the Ridge should have a star formation rate of $8 \times 10^{-3} M_\odot \text{ yr}^{-1}$, but the total $\text{H}\alpha$ and $24 \mu\text{m}$ emission in the Ridge suggests a star formation rate of only $2.6 \times 10^{-4} M_\odot \text{ yr}^{-1}$ (Calzetti et al. 2007). Indebetouw



Original content from this work may be used under the terms of the [Creative Commons Attribution 4.0 licence](#). Any further distribution of this work must maintain attribution to the author(s) and the title of the work, journal citation and DOI.

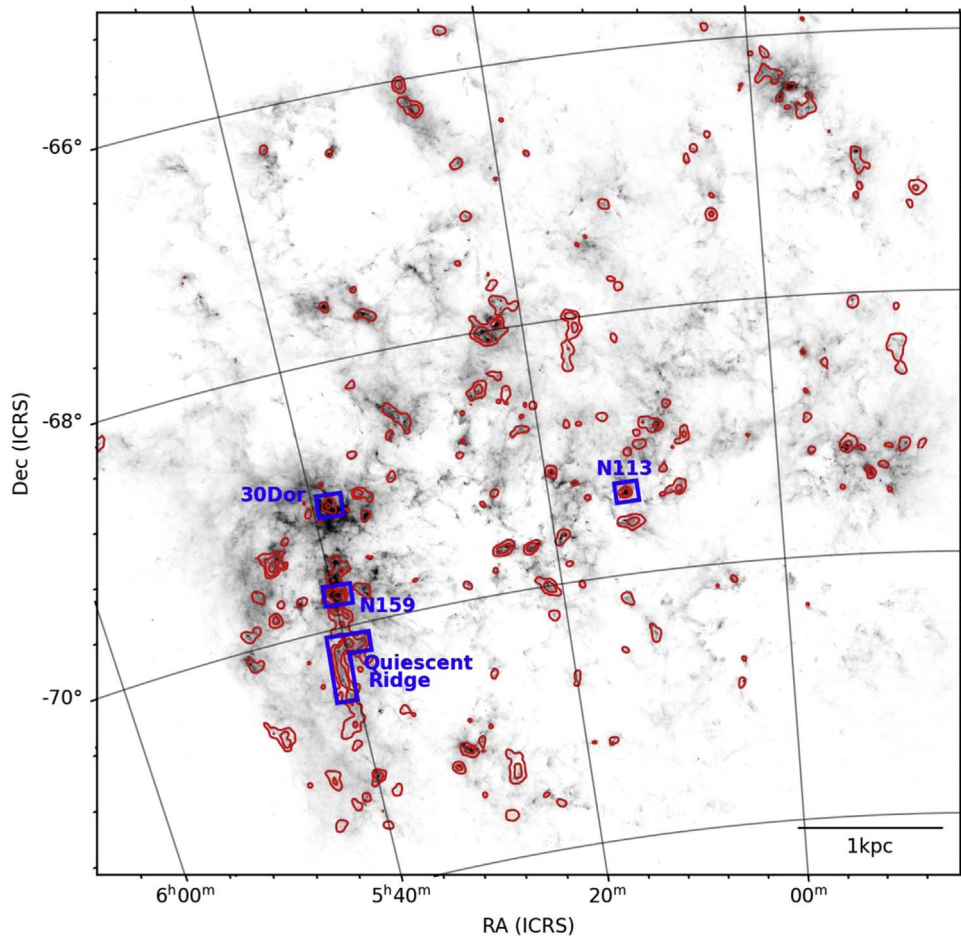


Figure 1. The LMC with the Molecular Ridge, 30 Dor, N159, and N113 highlighted in blue. The gray scale is PACS 250 μm from the HERITAGE survey (Meixner et al. 2013), and the red contours are ^{12}CO (1–0) from the NANTEN survey (Fukui et al. 2008) showing the extent of all the CO-bright molecular gas in the LMC. Levels are 1.6, 5, and 12 K km s^{-1} .

et al. (2008) found that these numbers can be better reconciled by looking for embedded young stellar objects (YSOs) from the Spitzer Space Telescope survey Spitzer Surveying the Agents of Galaxy Evolution (SAGE; Meixner et al. 2006), which brought the measured star formation rate to approximately $4 \times 10^{-3} M_{\odot} \text{ yr}^{-1}$, within a factor of two of the value predicted by the Schmidt–Kennicutt law. This suggests that the lack of $\text{H}\alpha$ and optical clusters is because the Ridge is preferentially forming low-mass star clusters.

This is a stark contrast to regions just north of the Ridge, such as 30 Dor and N159 (see Figure 1), which are some of the most active massive-star-forming regions in the LMC. 30 Dor is home to R136, the closest known super star cluster (SSC), and other young, massive clusters that bring the total mass of recently formed stars in the region up to $\sim 8.7 \times 10^4 M_{\odot}$ (Cignoni et al. 2015). There are still giant molecular clouds (GMCs) forming stars in the region, although the current star formation in 30 Dor is less extreme than it once was, forming primarily low- and intermediate-mass stars (Walborn et al. 2013; Sabbi et al. 2016). Just south of 30 Dor is N159, which contains several embedded high-mass YSOs and H II regions (Chen et al. 2010), suggesting that massive star formation is ongoing in this region. N113 similarly has signs of active high-mass star formation (Sewilo et al. 2010; Seale et al. 2012; Ward et al. 2016). By directly comparing the molecular gas in these regions with that in the Ridge, we hope to identify differences

in the physical conditions that could suggest why the regions differ so much in star-forming properties.

Finn et al. (2021) fit RADEX models to CO emission in the Ridge and found that the fitted volume density, n_{H_2} , had the strongest correlation with the presence of YSOs associated with the CO clumps. They hypothesized that the Ridge could be forming massive stars so sluggishly either because the molecular gas is lower density than the other star-forming regions to its north or because the threshold density for star formation is higher in the Ridge. For example, the latter could be caused by higher amounts of turbulent or magnetic support suppressing collapse in the Ridge.

In this paper, we seek to understand the underlying differences in physical conditions between the Ridge and the other massive-star-forming regions, 30 Dor, N159, and N113. In Section 2 we present the different observations and regions being compared in this analysis, and in Section 3 we describe how we segment that observed emission into smaller structures using both dendrogram and clump-finding methods. We calculate the mass, velocity dispersion, and radii of these structures in Section 4. We compare the different regions by fitting size–line width relations in Section 5 and by considering their virial balance of turbulent and gravitational energy in Section 6. We examine variations in these physical properties within the Ridge in Section 7 and look at the spatial dependence of those variations in Section 8. We bring the

Table 1
Observations Used in This Analysis

Region	Line	Beam (arcsec)	rms (K)	Velocity Resolution (km s ⁻¹)
Ridge	¹³ CO (1–0)	13	0.03	0.5
Ridge	CS (2–1)	18	0.017	0.5
30 Dor	¹³ CO (2–1)	13	0.009	0.25
N159	¹³ CO (1–0)	13	0.04	0.5
N113	¹³ CO (1–0)	13	0.0075	0.5

results of all of these sections together in Section 9 to discuss the overall picture of the differences in these regions, and then we summarize our conclusions in Section 10.

2. Observations

We examine the Molecular Ridge in ¹³CO (1–0) and CS (2–1) and compare it to three other regions in the LMC: 30 Dor, N159, and N113. The observations used in this analysis and their resolutions and measured rms are summarized in Table 1.

2.1. Molecular Ridge

The Molecular Ridge was observed by the Atacama Large Millimeter/submillimeter Array (ALMA) 7 m Atacama Compact Array (ACA) in three maps for project 2017.1.00271.S. This data set was combined with ALMA 7 m ACA projects 2012.1.00603.S and 2015.1.00196.S, which covered the $\sim 2'$ region around 5:39:50–70:08:00 in the northern center of the maps. These were all also combined with ALMA total power data. The data reduction, calibration, and imaging are described in detail in Finn et al. (2021). The final maps have a resolution of 13'' and a measured rms in line-free channels of 0.03 K. An integrated intensity map of the ¹³CO (1–0) and CS (2–1) emission is shown in Figure 2.

2.2. 30 Doradus

A mosaic of 30 Dor was observed as ALMA project 2019.1.00843.S and includes 12 m and 7 m interferometric data and total power data. Those data are presented and analyzed at their native resolution of 1''.75 in Wong et al. (2022). For this analysis, the resolution has been convolved to 13'' so that it can be directly compared with our data for the Molecular Ridge. After this convolution, the data have a measured rms in line-free channels of 0.009 K. This rms is much lower than the other data sets, but we find that removing structures below the Ridge's noise level of 0.03 K from the analysis does not significantly change the results. An integrated intensity map of these data is shown in Figure 3.

This data set is ¹³CO (2–1), rather than ¹³CO (1–0) like all the other regions. We use a ¹³CO (2–1)/¹³CO (1–0) ratio of 0.84 based on the ¹²CO (2–1)/¹²CO (1–0) ratio measured in Sorai et al. (2001).

2.3. N159

N159 is a massive-star-forming region to the north of the Ridge but south of 30 Dor. The brightest point in early single-dish surveys of CO in the LMC, this massive-star formation region is less evolved than 30 Dor and has a significant remaining reservoir of molecular gas. N159 can be separated into eastern and western components (N159E and N159W),

where N159E is thought to be more evolved than N159W (Nayak et al. 2018). There is also another region to the south called N159S that is much more quiescent and is not included in this study. Due to the small number of structures identified at this work's resolution, we treat N159E and N159W as a single region, and this does not significantly affect the results of our analysis.

N159 was observed in ¹³CO (1–0) by ALMA project 2012.1.00554.S with 12 m and 7 m interferometric data and was presented at the native resolution of 2.5'' \times 1.8'' in Fukui et al. (2015). These data do not include total power data, and so we expect a flux recovery around 66% based on data in the Ridge. We take this correction into account in the mass estimates. As with the other comparison data sets, we convolved the data to 13'' to match the Ridge data. After this convolution, the data have a measured rms in line-free channels of 0.04 K. An integrated intensity map of these data is shown in Figure 4.

2.4. N113

N113 is another active massive-star-forming region in the LMC with several young, embedded massive YSOs. It is located in the central region of the LMC. N113 was observed in ¹³CO (1–0) by ALMA project 2015.1.01388.S with 12 m interferometric data. These data do not include total power data, and so we expect a flux recovery around 66% based on data in the Ridge. We take this correction into account in the mass estimates. A complete description of the data processing will be discussed in a separate publication at the observations' native resolution of $\sim 2''$. For this work, the data were convolved to 13'' so they could be directly compared to our Molecular Ridge data. After this convolution, the data have a measured rms in line-free channels of 0.0075 K. This rms is much lower than the other data sets, but we find that removing structures below the Ridge's noise level of 0.03 K from the analysis does not significantly change the results. An integrated intensity map of these data is shown in Figure 5.

3. Structure Decomposition

To decompose the emission into structures, we used two different methods: splitting the emission into a hierarchy of structures called a dendrogram, and splitting the emission into individual, nonoverlapping clumps. Dendrograms better capture the complex and hierarchical nature of molecular clouds but complicate analysis because the emission is multiply counted and the resulting structures often defy the physics commonly used to describe molecular clouds (e.g., we report a single radius for molecular clouds, even though dendrogram structures are frequently nonspherical and have complex and elongated shapes). Clump-finding algorithms offer a simpler approach to analysis but are biased toward finding clump structures that are approximately round and the size of the beam, and they cannot capture the hierarchical structure of molecular clouds.

In this study, we use both types of structure decomposition depending on the type of analysis being performed. We use dendrogram structures for the majority of the analysis since they better capture the hierarchical nature of clouds and can demonstrate how the physical properties behave at different size scales. We use clumps for counting-based analyses, such as histograms, since dendrograms multiply count emission.

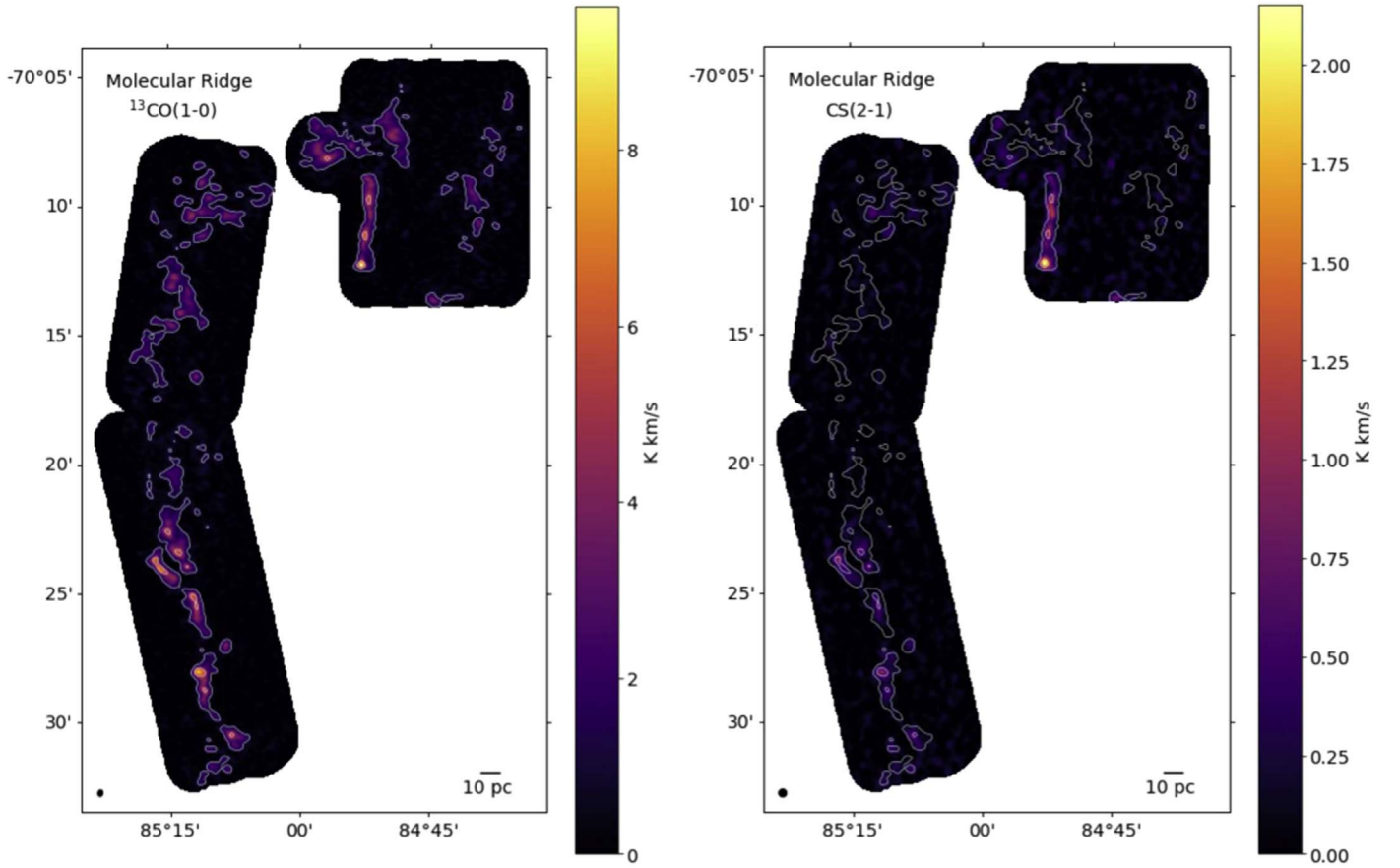


Figure 2. Left: integrated intensity map of the Molecular Ridge in ^{13}CO (1–0). Contours show 1, 5, and 9 K km s^{-1} . Right: integrated intensity map of the Molecular Ridge in CS (2–1), with the same contour lines from ^{13}CO (1–0) overplotted. In both images, the beam is shown in the lower left corner.

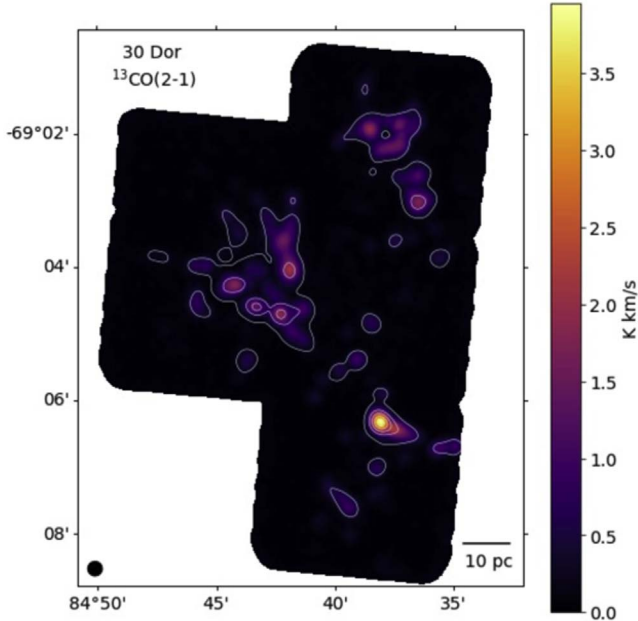


Figure 3. Integrated intensity map of 30 Dor in ^{13}CO (2–1). Contours show 1, 5, 9, 13, and 17 K km s^{-1} . The beam is shown in the lower left corner.

Due to its bias toward beam-sized structures, the clump segmentation method results in smaller ranges of masses, sizes, and line widths being calculated in Section 4. The ranges of

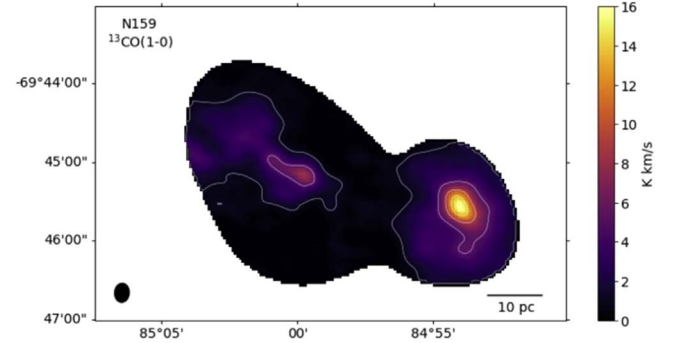


Figure 4. Integrated intensity map of N159 in ^{13}CO (1–0). Contours show 1, 5, 9, and 13 K km s^{-1} . The beam is shown in the lower left corner.

these parameters for the identified clumps align most closely with those for the leaves of the dendrogram.

3.1. Dendrogram Segmentation

We decompose the emission in each map into structures using the package *astrodendro* (Rosolowsky et al. 2008) to create a dendrogram. This method of structure decomposition considers how different structures within the data merge as you go to lower contour levels to create a hierarchical categorization of the structures. We used input parameters of $\text{min_value} = 3\sigma$, $\text{min_delta} = 2.5\sigma$, and $\text{min_npix} = 2$ beams, meaning that the algorithm includes only pixels that are above 3σ and finds local maxima that are at least 2.5σ above

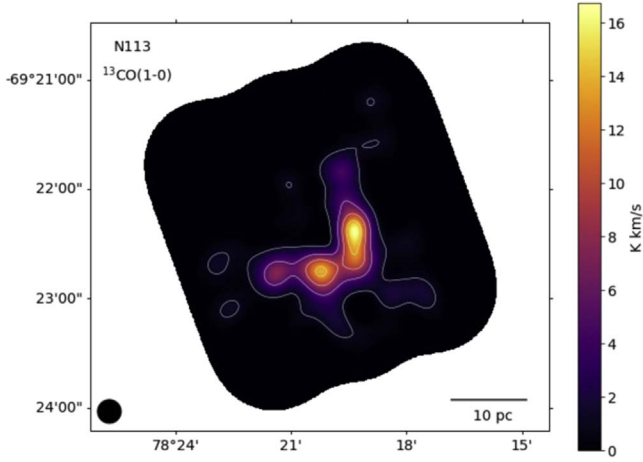


Figure 5. Integrated intensity map of N113 in ^{13}CO (1–0). Contours show 1, 5, 9, and 13 K km s^{-1} . The beam is shown in the lower left corner.

the point of merging with another structure and bounded by an isosurface with at least as many voxels as two resolution beams.

The local maxima with no resolved substructure are categorized as “leaves.” The algorithm then identifies the points at which these structures merge to define larger structures, categorized as “branches” and “trunks,” where trunks are the largest structures that are not bounded by any other structures. Figure 6 shows the dendrogram for emission in the Ridge using the above parameters, and the breakdown in dendrogram structures for each region is shown in Table 2.

3.2. Clump Segmentation

To decompose emission into clumps, we use the algorithm `quickclump` (Sidorin 2017). We used the input parameters $N_{\text{levels}} = 1000$, $T_{\text{cutoff}} = 4\sigma$, $dT_{\text{leaf}} = 4\sigma$, and $N_{\text{pixmin}} = 50$. The resulting numbers of clumps for each region are shown in Table 2.

3.3. Fractal Dimension

It is widely found that molecular gas is encountered in fractal structures (i.e., Elmegreen & Falgarone 1996) and that this fractal nature is connected to supersonic turbulence in the interstellar medium (Elmegreen et al. 2001). We consider whether the emission in the Ridge has a fractal morphology that is similar to the morphology in 30 Dor and N113 by measuring the fractal dimension, D_2 , of the structures identified by the dendrogram segmentation in each region. We do this with the area–perimeter relation, $P \propto A^{D_2/2}$ (Falgarone et al. 1991). We measure the perimeter and the area of each structure based on the full contour defined by the `astrodendro` algorithm for the Ridge, 30 Dor, and N113 and then fit a power law to each data set using a nonlinear least-squares method (`scipy.optimize.curve_fit`; Virtanen et al. 2020). We do not include N159 because the emission on the edges is cut off by the observed map. We fit only the structures that have an area larger than the size of the beam, which is 45 pc^2 . The resulting fits are shown in Figure 7.

Each of the data sets are consistent with one another given the error, having fractal dimensions of $D_2 = 1.50 \pm 0.02$, 1.44 ± 0.02 , and 1.42 ± 0.07 for the Ridge, 30 Dor, and N113, respectively. This suggests that the three regions have

a similar hierarchical morphology and so likely have similar mechanisms by which turbulence regulates cloud structure.

These values are higher than the $D_2 = 1.36 \pm 0.02$ measured in galactic molecular clouds with ^{12}CO by Falgarone et al. (1991) but are consistent with the range of 1.2–1.5 measured for HI emission in galactic clouds by Sánchez et al. (2007). These values are also consistent with similar measurements made using stellar structures in the LMC (Miller et al. 2022) and the Small Magellanic Cloud (SMC; Sun et al. 2018), where both find $D_2 = 1.44 \pm 0.2$.

4. Derived Properties

To compare the physical conditions of the molecular clouds in each region, we compute the mass, line width, radius, and virial parameter α_{vir} for each structure in each region.

We calculate the mass using an $X_{^{13}\text{CO}}$ factor to convert from integrated ^{13}CO (1–0) intensity to H_2 column density. We adopt a value for $X_{^{13}\text{CO}}$ of $1.6 \times 10^{21} \text{ cm}^{-2} (\text{K km s}^{-1})^{-1}$ based on Finn et al. (2021) measurements of non-LTE model-fitted column density in the Ridge. Finn et al. (2021) found that the non-LTE fitted column density of clumps was tightly correlated with the ^{13}CO (1–0) integrated emission, even more so than with the ^{12}CO (1–0) integrated emission. This value of $X_{^{13}\text{CO}}$ is also consistent with using a typical galactic X_{CO} factor of $2 \times 10^{20} \text{ cm}^{-2} (\text{K km s}^{-1})^{-1}$ (Bolatto et al. 2013) and a ^{13}CO (1–0)/ ^{12}CO (1–0) integrated intensity ratio of 0.12 (Finn et al. 2021). The resulting column densities for 30 Dor also match the ranges of those calculated using LTE assumptions in Wong et al. (2022).

We adopt an error of 10% on the calculated masses based on an assumed 10% flux calibration error (Fomalont et al. 2014). The error associated with the measured σ_{rms} of the image is negligible compared to the flux calibration error. Adopting an $X_{^{13}\text{CO}}$ factor also comes with a large systematic error. Finn et al. (2021) cite an error of 50% based on systematic uncertainties in the $\text{H}_2/^{13}\text{CO}$ abundance ratio, which is added in quadrature to the 10% flux error. The structures in 30 Dor have an additional systematic error since we only have observations of ^{13}CO (2–1), and so we use a ^{13}CO (2–1)/ ^{13}CO (1–0) ratio of 0.84 ± 0.3 (Sorai et al. 2001).

To calculate the line width of each structure, we fit a Gaussian to the intensity-weighted mean line profile to determine σ_v (not the FWHM). This line width is then deconvolved with the velocity resolution of the data sets (either 0.5 or 0.25 km s^{-1} ; see Table 1). To find the error in the measured line widths, we create 100 noise maps that have been convolved to the same beam size and have the same σ_{rms} as the emission maps, add these to the data, and then recompute the line width. The error is taken to be the standard deviation in the measured line widths with the added noise.

We performed the above method of error calculation for N159, N113, and 30 Dor, but this was not computationally feasible for the Ridge owing to the large size of the data cube and number of clumps. Instead, we found that the fractional error in σ_v ($\sigma_{\sigma_v}/\sigma_v$) from this method in N159, N113, and 30 Dor is closely correlated with the peak brightness temperature (T_{max}) of the structure. We fit this correlation and extrapolated it to the Ridge data set to determine approximate

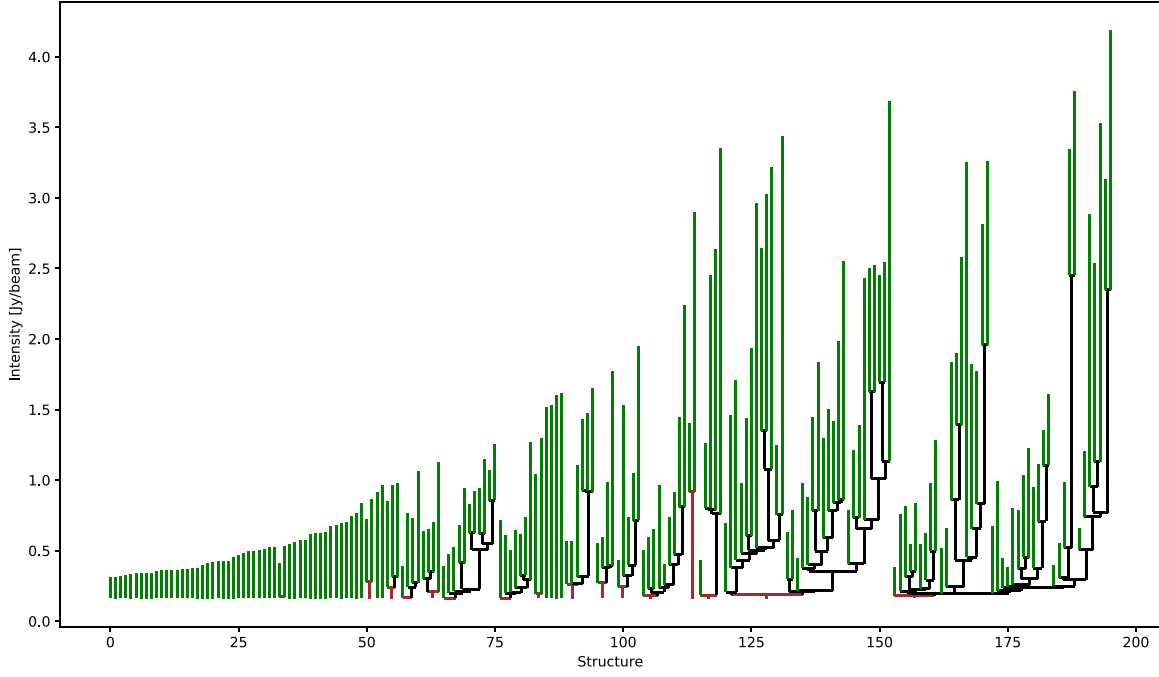


Figure 6. Dendrogram for the Ridge created by *astrodendro*. Each structure is represented by a vertical line, where the green lines are leaves, black lines are branches, and red lines are trunks. The y-axis indicates the peak of each structure and the intensity at which the structures merge with one another. This plot shows that the Ridge is composed of a few large trunks with a lot of substructure, but also several smaller and more isolated structures.

Table 2

Results of Dendrogram and Clump Segmentation, and Fractal Dimension, D_2 , for Each Region

Region	Trunks	Branches	Leaves	Clumps	D_2
Ridge ^{13}CO	16	110	196	256	1.50 ± 0.02
Ridge CS	4	6	34
30 Dor ^{13}CO	6	45	96	75	1.44 ± 0.02
N159 ^{13}CO	1	4	7	9	...
N113 ^{13}CO	1	6	10	10	1.42 ± 0.07

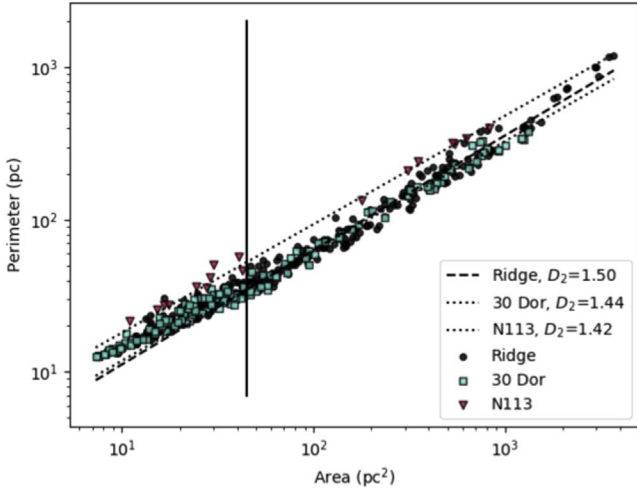


Figure 7. Perimeter plotted against area of the full contours for dendrogram structures identified in the Ridge, 30 Dor, and N113. We fit power laws to each region to measure the fractal dimension, D_2 , with the area–perimeter relation, $P \propto A^{D_2/2}$. We fit only structures that are larger than the area of the beam, 45 pc, represented by the vertical line. All of the data sets are consistent with one another, suggesting that they have a similar hierarchical morphology.

errors for each structure using the following fitted equation:

$$\log\left(\frac{\sigma_v}{\sigma_v}\right) = -0.69 \log(T_{\max}/\text{K}) - 2.23. \quad (1)$$

To calculate the sizes, we fit an ellipse to the half-power contour of the structure. To get a single radius value, we used the geometric mean of the major and minor axes of this fitted ellipse, which is then deconvolved with the beam size for the data set. This value is taken to be a half-width at half-maximum (HWHM) of the structure, from which we approximated $\sigma_R = \text{HWHM} \times 2/2.35$. We then multiplied σ_R by a factor of 1.91 (Solomon et al. 1987) to get our quoted “effective radius,” R . The error was determined with the same method used for the error in the line width. In the case of the radius, the fractional errors from N159, N113, and 30 Dor are also closely correlated with the peak brightness temperature (T_{\max}) of the structure, and this fitted correlation was extrapolated to the Ridge to approximate errors with the equation

$$\log\left(\frac{\sigma_R}{R}\right) = -1.09 \log(T_{\max}/\text{K}) - 1.60. \quad (2)$$

Deconvolving the radius with the beam and the line width with the velocity resolution resulted in some data points being dropped from the analysis because the half-power contour is smaller than the beam or the fitted line width is smaller than the velocity resolution. This left us with 204 structures in the Ridge, 51 structures in 30 Dor, and 9 structures each in N159 and N113.

For N159 and N113, we adopt an additional correction factor of 1/0.66 in the measured masses to account for the lack of total power data, which we expect to result in a flux recovery of 66% based on data from the Ridge that includes total power. We find that leaving out the total power data in the Ridge does not significantly affect the measured radii or line widths of the structures.

The three parameters above, mass (M), radius (R), and line width, σ_v , are used to calculate the virial parameter, α_{vir} , as a measurement of the balance between gravity and outward pressure, calculated for a spherical cloud. Most molecular cloud structures that we observe are not spherical, which could influence the value of α_{vir} by a factor of order unity. Values of α_{vir} greater than 1 indicate that the cloud is dominated by kinetic energy, which could mean that the cloud is not bound and will disperse, or that it is constrained by an external pressure to keep it bound. The kinetic energy could also be dominated by potential energy because the cloud is in freefall collapse. Values of α_{vir} less than 1 indicate that the cloud is dominated by potential energy and so is likely to begin collapse. We use the equation

$$\alpha_{\text{vir}} = \frac{5\sigma_v^2 R}{GM}. \quad (3)$$

The parameters derived in this section are used in the following sections for the remainder of the analysis. Throughout the analysis, we use the properties derived from ^{13}CO emission rather than CS unless specified otherwise.

5. Size–Line Width Relations

We plot the ^{13}CO line widths of all the structures against their effective radii. The relation between the two is expected to follow a power law (Larson 1981; Solomon et al. 1987) of the form

$$\sigma_v = a_0 R^{a_1}. \quad (4)$$

Solomon et al. (1987) measured sizes and line widths for molecular clouds in the Galactic disk using a size parameter, S , instead of the effective radius, R , that we use in this study. The size parameter is the geometric mean of the spatial dispersions, σ_l and σ_b , of each cloud and so is comparable to the σ_R that we measured and then converted to effective radius with the equation $R = 1.91\sigma_R$ (see discussion in Section 4). Solomon et al. (1987) fit values of $a_0 = 1.0 \pm 0.1$ and $a_1 = 0.5 \pm 0.05$, so converting their size parameter to an effective radius would result in an intercept for the power law of $a_0 = 0.72 \pm 0.07$.

In Figure 8, we plot the radius and velocity dispersion of the structures and fit both the intercept and slope, a_0 and a_1 , for the Ridge and 30 Dor, using an orthogonal distance regression to take into account the error in both axes (`scipy.odr`; Virtanen et al. 2020). We do not fit these values for N159 and N113 since there are so few data points and the fits are poorly constrained.

For the Ridge, we fit values of $a_0 = 0.41 \pm 0.03$ and $a_1 = 0.44 \pm 0.03$, while for 30 Dor we fit values of $a_0 = 0.72 \pm 0.11$ and $a_1 = 0.56 \pm 0.07$. This indicates that 30 Dor follows a steeper power law than the Ridge, although the two values of a_1 are within 3σ of each other. This means that 30 Dor may have more kinetic energy at larger size scales than the Ridge. The power-law slope we fit for 30 Dor structures ($a_1 = 0.56 \pm 0.07$) is comparable to those fit by Nayak et al. (2016), Wong et al. (2019), Indebetouw et al. (2020), and Wong et al. (2022) for dendrogram structures identified in ^{12}CO (2–1) and ^{13}CO (2–1) emission at resolutions ranging from 0.1 to 0.85 pc.

In Figure 9, we plot again the size and line width of the structures, but we now hold the slope of the power law fixed at $a_1 = 0.5$ (Solomon et al. 1987) and fit only the intercept, a_0 . In this case, we fit a value of $a_0 = 0.35 \pm 0.01$ for the Ridge,

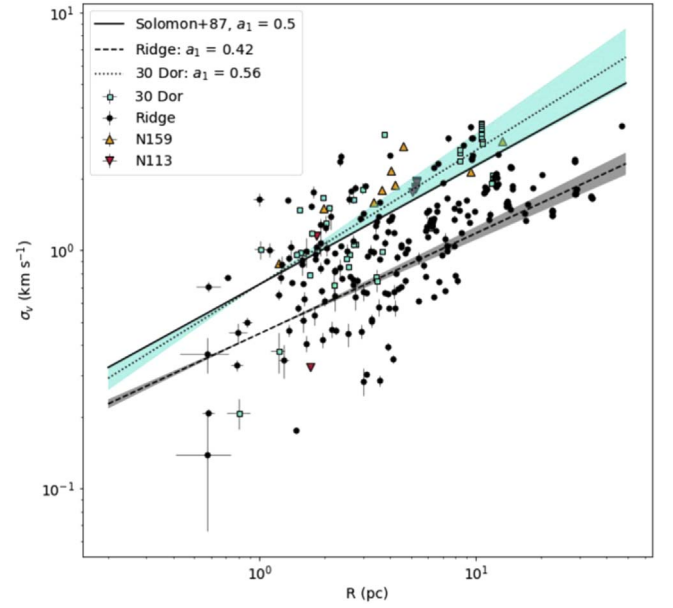


Figure 8. Line widths plotted against sizes of structures in the four different regions: the Ridge (black circles), 30 Dor (blue squares), N159 (orange upward-facing triangles), and N113 (red downward-facing triangles). A power law has been fit to the structures in the Ridge (dashed line) and 30 Dor (dotted line), with the error in the fit shown as shaded regions, and the value of the fitted power-law slope, a_1 , is written in the legend for each region. We do not fit power laws for N159 and N113 since their small numbers of data points cannot constrain the parameters well. The relation fit by Solomon et al. (1987) for Milky Way clouds is shown as a solid line, where $a_0 = 0.72$ and $a_1 = 0.5$. This indicates that 30 Dor follows a steeper power law than the Ridge, so it may have more kinetic energy at larger size scales than the Ridge, although the two values of a_1 are within 3σ of both each other and the fit by Solomon et al. (1987).

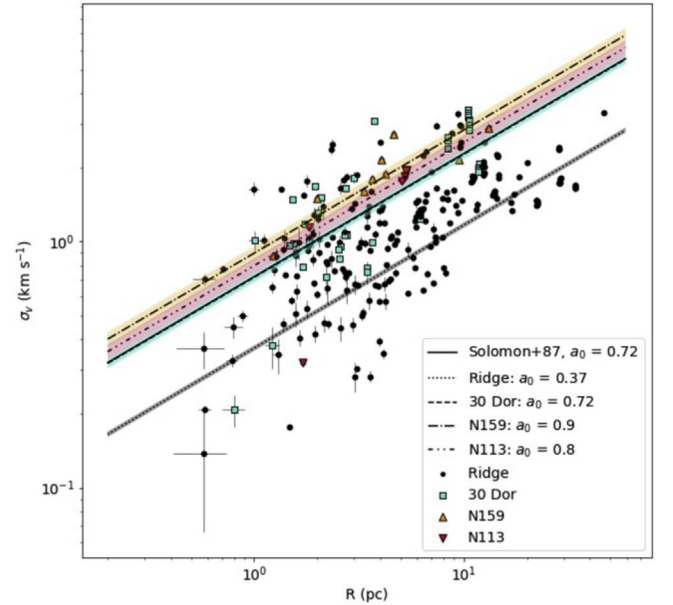


Figure 9. Line widths plotted against sizes of structures in the four different regions: the Ridge (black circles), 30 Dor (blue squares), N159 (orange upward-facing triangles), and N113 (red downward-facing triangles). A power law with a fixed slope of $a_1 = 0.5$ has been fit to the structures in each region, the error on each fit is shown as shading colored according to the region, and the value of the fitted power-law intercept, a_0 , is written in the legend for each region. The relation fit by Solomon et al. (1987) for Milky Way clouds is shown as a solid line, where $a_0 = 0.72$. The Ridge has a significantly lower fitted intercept than the other three regions, indicating that it has much less kinetic energy for a given size scale.

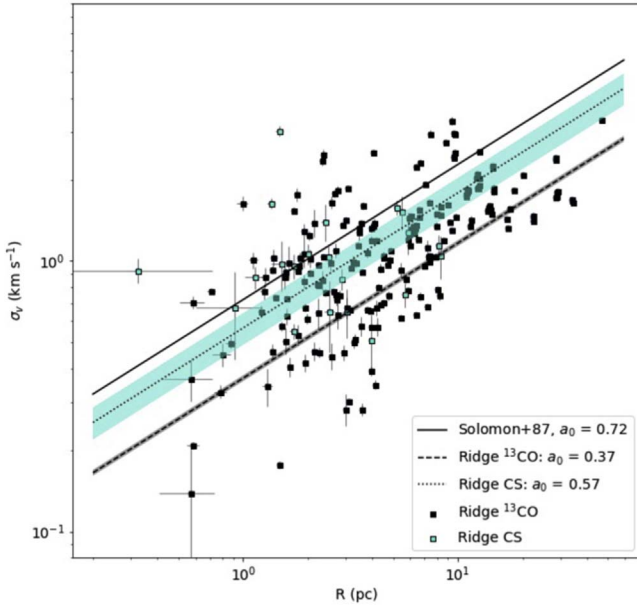


Figure 10. Line widths plotted against the sizes of structures in the Ridge identified by ^{13}CO (1–0) (black) and CS (2–1) (blue). We fit a power law with a fixed slope of $a_1 = 0.5$ to each, which shows that the CS (2–1) structures have a significantly higher fitted intercept than the ^{13}CO (1–0) structures. This indicates that the dense gas traced by CS (2–1) has higher kinetic energy at a given size scale.

$a_0 = 0.72 \pm 0.03$ for 30 Dor, $a_0 = 0.90 \pm 0.06$ for N159, and $a_0 = 0.80 \pm 0.05$ for N113. Changing the value of the fixed slope changes the fitted values of the intercept slightly but does not change the relative differences between data sets. The results above are also unchanged if we use clump-segmented structures instead of dendrogram structures.

The Ridge’s significantly lower intercept from the other three data sets indicates that it has less kinetic energy at a given size scale than the massive-star-forming regions. This result suggests that the lack of massive-star formation in the Ridge cannot be caused by excess kinetic energy suppressing star formation. This is quite different from the situation in the Galactic Center, where star formation is also suppressed but the molecular clouds have much higher kinetic energies ($a_0 = 3.0 \pm 0.7$ after converting the size parameter to an effective radius; Oka et al. 2001) than clouds in the disk of the Galaxy ($a_0 = 0.72 \pm 0.07$; Solomon et al. 1987). This indicates that while both regions are examples of deviations from star formation scaling laws, the physical drivers of that suppression are different.

5.1. Size–Line Width Relation with CS

In Figure 10 we plot the size and line width of the structures in the Ridge in ^{13}CO (1–0) and CS (2–1) and compare the fitted power-law intercept with a fixed slope of $a_1 = 0.5$. The structures from CS (2–1) have a fitted intercept of $a_0 = 0.57 \pm 0.08$, higher than the ^{13}CO (1–0) structure in the Ridge but within 3σ of the $a_0 = 0.35 \pm 0.01$ fitted above. This demonstrates that the dense gas structures traced by CS (2–1) in the Ridge have a higher kinetic energy than the more diffuse gas traced by ^{13}CO (1–0).

It is expected that measuring the sizes and line widths in a dense gas tracer as opposed to ^{13}CO would result in a size–line width relation with a higher intercept (Goodman et al. 1998).

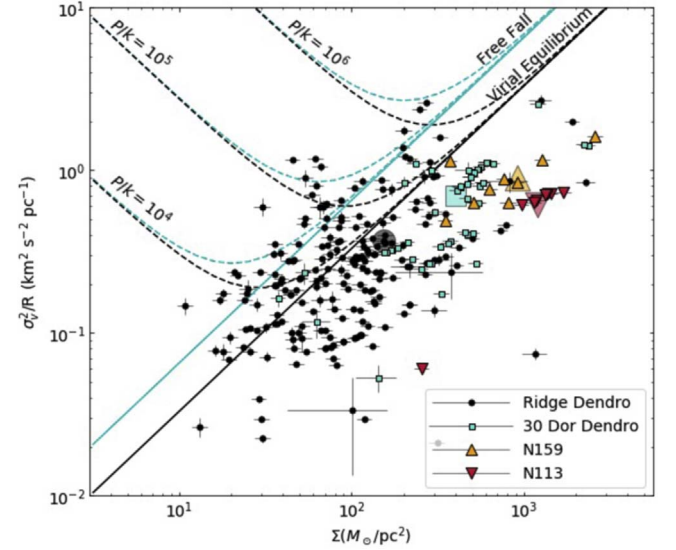


Figure 11. Surface density plotted against the velocity metric, σ_v^2/R , for the Ridge, 30 Dor, N159, and N113. The black line shows virial equilibrium, the blue line shows how equilibrium shifts when clouds are in freefall, and the dashed lines show those same quantities but when an external pressure is applied (Field et al. 2011). The large, semitransparent symbols corresponding to each region indicate the average surface density and velocity metric for each region. The systematic uncertainties for all data points are shown in the legend. The structures in the massive-star-forming regions appear to fall below the line of virial equilibrium more than the structures in the Ridge.

However, it is not clear from this plot alone what is causing the higher energy levels in the case of the Ridge presented here. It could be because the gas traced by CS (2–1) is found at the dense centers of clumps throughout the Ridge, where the higher kinetic energy is balanced by a higher gravitational potential. Or it could be that the areas of the Ridge that have CS (2–1) detections are sites where there is more star formation and gravitational collapse occurring, and so those areas have higher kinetic energies than the rest of the Ridge. Finn et al. (2021) see some correlation between the presence of YSOs and the CS (2–1)/ ^{12}CO (1–0) ratio in the Ridge, suggesting some support for the latter scenario, or that a combination of these two effects is at play.

6. Virialization

In Figure 11, we plot σ_v^2/R against the surface density of each structure. The positions of the structures on this plot indicate the balance between their gravitational potential energy and kinetic energy due to turbulence and temperature. If those two are in virial equilibrium, the structures should fall along the virial line, shown in black in Figure 11.

Due to the large systematic uncertainties in the measurements of the structures’ masses, the absolute positions relative to virial equilibrium on the plot are ambiguous. Instead, we focus this analysis on the relative positions of the data points from different regions. The Ridge structures tend to fall above virial equilibrium more often than structures in the massive-star-forming regions 30 Dor, N159, and N113—28% of the Ridge structures fall above the virial equilibrium line, whereas for 30 Dor that fraction is only 3%, and none of the structures in N159 or N113 fall above the virial equilibrium line.

To more quantitatively compare the balance of kinetic and gravitational energy in the Ridge and 30 Dor, Figure 12 shows the distribution of α_{vir} values in the two regions. Because

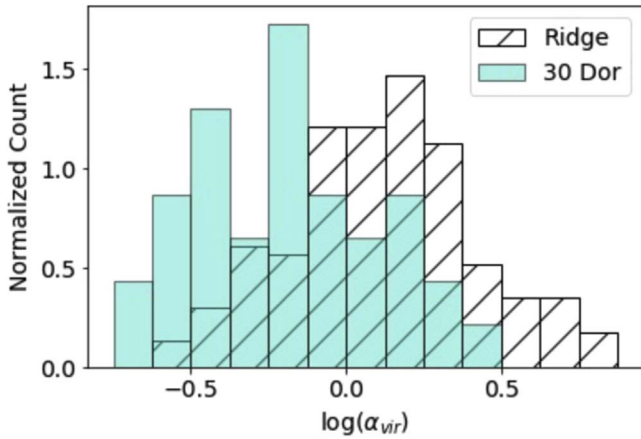


Figure 12. Distribution of α_{vir} values in the Ridge and 30 Dor, showing that the Ridge tends toward higher values of α_{vir} than 30 Dor. A K-S test indicates that the two data sets are not drawn from the same distribution with a p -value of $\ll 0.01$.

dendrograms multiply count emission, we use structures from `quickclump` to create all histograms in this analysis. Figure 12 clearly shows a difference in α_{vir} values between the two regions, with the Ridge structures tending toward higher α_{vir} . A Kolmogorov–Smirnov (K-S) test indicates that the two data sets are likely not drawn from the same distribution with a p -value of $\ll 0.01$.

We infer from Figure 9 that structures in the Ridge have lower kinetic energies than structures in 30 Dor. That means that for the Ridge to have higher α_{vir} values than 30 Dor, it must have much lower surface densities. In Figure 13, we show the distributions of surface densities in the Ridge and 30 Dor, and we do indeed see that those in the Ridge are significantly lower than those in 30 Dor, with a K-S test p -value of $\ll 0.01$. This suggests that the Ridge may be forming fewer massive stars compared to other regions because the Ridge does not have as much dense gas.

Given the much lower star formation activity in the Ridge and applying the Schmidt–Kennicutt law (Kennicutt 1998), it is expected that the surface density in the Ridge is lower than in 30 Dor. However, it is still higher than what would be predicted with the Schmidt–Kennicutt law based on the star formation rate measured in the Ridge by Indebetouw et al. (2008), $4 \times 10^{-3} M_{\odot} \text{ yr}^{-1}$. From that rate, we would expect a surface density of $\sim 47 M_{\odot} \text{ pc}^{-2}$, but here we measure a mass-weighted average surface density of $\sim 100 M_{\odot} \text{ pc}^{-2}$ in the Ridge. This demonstrates that while the Ridge is lower in surface density than 30 Dor, there is still a discrepancy with the Schmidt–Kennicutt law in the Ridge.

We compare these measured surface densities to the often-cited threshold for massive-star formation of $A_V > 8$ mag measured by Lada et al. (2010). Finn et al. (2019) calculate that, based on measurements of $\frac{A_V}{N_{\text{H}}}$ in the LMC (Dobashi et al. 2008), this threshold would correlate to $\Sigma_{\text{gas}} > 490 M_{\odot} \text{ pc}^{-2}$. Plotting this threshold on Figure 13 indicates that the majority of structures in the Ridge fall below this threshold, while 30 Dor structures are distributed around this threshold and have a mass-weighted average of $500 M_{\odot} \text{ pc}^{-2}$. There were too few structures in N159 and N113 at this resolution to include them in a histogram, but their mass-weighted average surface densities were 1100 and $1260 M_{\odot} \text{ pc}^{-2}$, respectively. This is all consistent with the Ridge having little massive-star

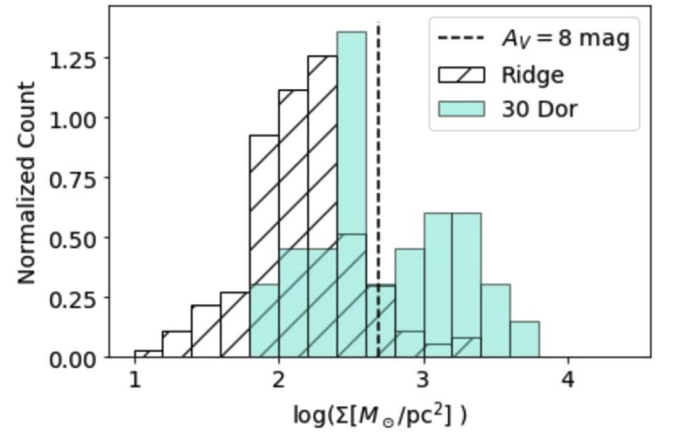


Figure 13. Distribution of surface densities in the Ridge and 30 Dor. The Ridge has significantly lower surface densities than 30 Dor, which results in structures in the Ridge having higher α_{vir} values despite their lower kinetic energies. Also shown is the $A_V > 8$ mag threshold for massive-star formation from Lada et al. (2010), converted to $\Sigma_{\text{gas}} > 490 M_{\odot} \text{ pc}^{-2}$. This indicates that the Ridge is likely not forming massive stars because it lacks dense gas.

formation because it falls below a density threshold compared to the other massive-star-forming regions.

It is expected that highly irradiated clouds, such as those in 30 Dor close to R136, will have a higher dark-gas fraction due to photodissociation and so a higher X_{CO} factor (Chevance et al. 2020). This effect would also cause us to see less of the diffuse envelope of the cloud, meaning that both the measured radii and line widths may be underestimated. O’Neill et al. (2022) make a thorough study of the effect of CO-dark gas on the measured properties of clouds. Their analysis suggests that in extreme cases of compactness for clouds in 30 Dor, the discrepancy in Figure 11 could be explained by a significantly higher dark-gas fraction than in the Ridge. However, the effect of CO-dark gas on the size–line width relation, such as is shown in Figure 9, would be to move up and to the right, mostly parallel to the relation. This suggests that it is quite unlikely that the difference in fitted a_0 intercept values is due to differences in the amount of CO-dark gas in the regions. Differences in the abundance ratio of ^{13}CO would cause similar effects, but the abundances have not been measured well enough to make any strong comment on this effect.

The use of ^{13}CO (2–1) in 30 Dor and ^{13}CO (1–0) in the Ridge and the other regions likely also affects their relative distributions of α_{vir} , even after applying a correction factor of ^{13}CO (2–1)/ ^{13}CO (1–0) = 0.84 to the 30 Dor masses. Since we expect ^{13}CO (2–1) to be fainter and not as well detected as ^{13}CO (1–0), this probably has a similar effect to that of CO-dark gas, although a thorough study taking into account excitation would be necessary to draw any firm conclusions.

7. Variation within the Ridge

To further investigate the physical conditions in the Ridge, we next look for variation in α_{vir} values and other physical properties within the region. Figure 14 shows a map of the Ridge colored by the α_{vir} parameter measured for the structure. In this map, we use structures found with `quickclump` to minimize overlap in the map. Where there is overlap along the line of sight, the average is shown. Also shown in the map are YSOs from Whitney et al. (2008), Gruendl & Chu (2009), and Seale et al. (2014), as well as H II regions and their sizes from Henize (1956). There appear to be some regions that tend

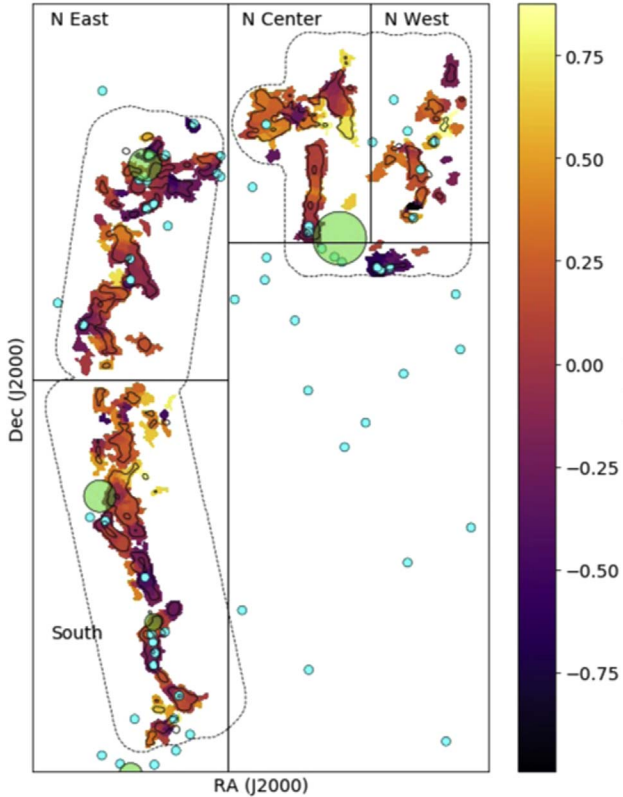


Figure 14. Map of the Molecular Ridge colored by each structure’s α_{vir} parameter. For this map we used structures found with `quickclump` to minimize structure overlap. Where there is overlap along the line of sight, we show the average α_{vir} . The small blue circles indicate YSOs from infrared surveys (Whitney et al. 2008; Gruendl & Chu 2009; Seale et al. 2014), and the large green circles indicate H II regions and their sizes from Henize (1956). The black lines show the boundaries used to split the Ridge into four different regions to analyze, and the dashed lines show the observation footprint.

toward higher or lower α_{vir} parameters, but there does not seem to be any consistent trend north to south along the Ridge.

We split the structures in the Ridge into four main regions—a southern region, and then an eastern, a central, and a western region to the north (hereafter referred to as NE, NC, and NW, respectively). The boundaries between these regions are shown in Figure 14. There is one major clump not included in any region, just below the borders of the NC and NW regions. This clump is partly cut off by the edge of the observation footprint and so does not have a reliable α_{vir} measurement. It is left out of the analysis.

To compare the α_{vir} values in each of the four regions, we plot histograms of their values in Figure 15. The shapes of these distributions appear by eye primarily Gaussian. We perform a K-S test on each pairing of regions to determine whether their values of α_{vir} are drawn from a common distribution. The resulting p -values of the K-S test for each pairing are presented in Table 3, where a p -value of less than 0.05 means we reject the null hypothesis (that the α_{vir} values for the two regions are drawn from the same distribution) with at least 95% confidence.

The South, NC, and NW regions are all consistent with being drawn from the same distribution. The NE region, however, has K-S test p -values less than 0.05 when paired with each of the other regions, suggesting that its α_{vir} values are not drawn from the same distribution. This suggests that there is a difference in

the physical conditions in the NE region that is causing lower values of α_{vir} in that region compared to the rest of the Ridge.

We look into this difference further by comparing the size–line width relation in these different regions within the Ridge. Similar to Section 5, we fit the power-law relation between σ_v and R for the structures in each of these regions with the slope of the power law fixed at $a_1 = 0.5$ (Figure 16). For these regions, we fit $a_0 = 0.33 \pm 0.01$, 0.35 ± 0.01 , 0.55 ± 0.03 , and 0.46 ± 0.03 for the South, NE, NC, and NW regions, respectively. This indicates that the South and NE regions have similarly low kinetic energies, while the NW region has higher kinetic energy and the NC has the highest kinetic energy. This makes sense since the NC region hosts the large H II region N171 (Henize 1956).

The low kinetic energy in the NE region relative to the NC and NW regions could explain why its α_{vir} values are lower. However, the kinetic energy in the South region appears nearly as low, and its α_{vir} values are comparable with those in the NC and NW regions. To explain these variations in α_{vir} values, we also consider maps of n_{H_2} in the Ridge based on fitting RADEX models to low-resolution ^{12}CO and ^{13}CO emission in Finn et al. (2021). This map indicates that the NE region has higher gas densities than the South region, which would result in the NE having lower α_{vir} values despite having comparably low kinetic energy. It is unclear from these plots what might be causing the higher densities in the NE region.

8. Spatial Dependence

To investigate what is driving the variations in α_{vir} values in the Ridge, we consider how α_{vir} varies with proximity to the nearest YSO, to the nearest H II region, and to R136 in 30 Dor. These plots are shown in Figure 17, and for each we calculate a Pearson’s correlation coefficient, r .

All three of these show similarly weak correlations. The variation of α_{vir} with distance to R136 shows the weakest correlation, with a coefficient of -0.27 . This agrees with our by-eye assessment of Figure 14 that there appears to be little cohesive north-to-south trend across the Ridge. This result suggests that the super star cluster R136 and in general the massive-star formation to the north are not strongly affecting the physical conditions in the Ridge at this distance. This is consistent with the findings of Wong et al. (2022) that there is little correlation with α_{vir} for clouds in 30 Dor and their distance to R136.

The weak correlation in the figure appears most dominated by lower α_{vir} values around a distance of 1.1 kpc from R136, which corresponds to a decl. of approximately $-70^\circ 26' 4$. This falls halfway along the South region defined in Figure 14 and is near several YSOs and an H II region.

The correlation coefficient between α_{vir} and distance to the nearest YSO is 0.29, and that between α_{vir} and distance to the nearest H II region is 0.28. The weak correlation suggests that local influences such as radiation and thermal pressure from nearby star formation have a small effect on molecular gas conditions. Structures that have a nearby YSO or H II region tend to have lower α_{vir} . This could be because the YSOs and H II regions are creating gas conditions that are conducive for further star formation, or because they are more likely to be associated with gas that has the right conditions for star formation.

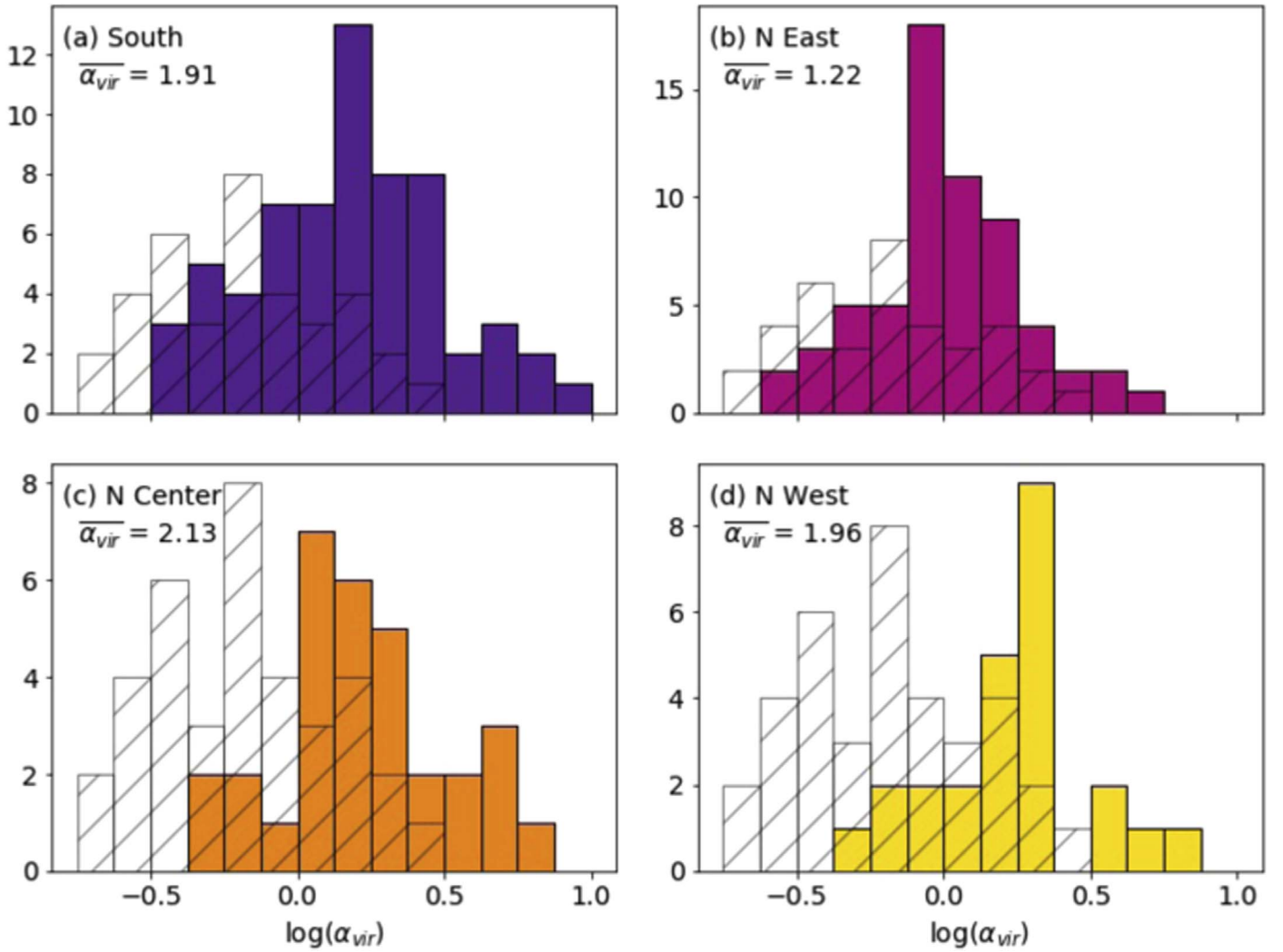


Figure 15. Histograms of the α_{vir} parameter by region in the Ridge, derived from ^{13}CO (1–0) (Figure 14 shows the extent of the regions). Overplotted in black hatching is the α_{vir} distribution of 30 Dor. The average α_{vir} parameter is shown in the upper left corner of the panel for each region. A series of K-S tests indicate that the NE region (pink) has a different distribution than each of the other regions in the Ridge. The NE region tends toward lower values of α_{vir} than the rest of the Ridge.

Table 3

K-S Test p -values of α_{vir} Distributions in Pairings of Regions within the Ridge, Derived from ^{13}CO (1–0)

	N East	N Center	N West
South	0.016	0.702	0.305
N East	...	0.002	0.001
N Center	0.751

9. Discussion

With this analysis, we hope to better understand what is driving the differences in star formation activity between the Molecular Ridge and the nearby massive-star-forming regions 30 Dor, N159, and N113. By comparing the fractal dimensions of 30 Dor and the Ridge, it seems that the hierarchical morphology in the two regions is similar and thus the state of fragmentation is not driving the difference in star formation.

From Figure 8, we conclude that the Ridge has significantly lower kinetic energy per size scale than the massive-star-forming regions, while Figure 12 demonstrates that despite the low kinetic energy, the Ridge still has higher values of α_{vir} on average. This must be driven by relatively low surface densities

in the Ridge, which is confirmed by Figure 13. All of this evidence suggests that the Ridge’s lack of massive-star formation is likely driven by a paucity of dense gas relative to regions like 30 Dor, rather than collapse being suppressed by excess turbulence in the Ridge. However, as Finn et al. (2021) point out, surface density cannot account for differences in line-of-sight length and cannot directly trace the true volume density of the gas. To directly compare the volume density of the gas in the Ridge and the massive-star-forming regions, we would need to observe multiple ^{12}CO and ^{13}CO emission lines in other regions and perform the same RADEX fitting done in Finn et al. (2021).

As shown in Figure 11, the systematic uncertainty in the mass estimates makes it difficult to discuss the absolute position of the structures relative to virial equilibrium. The Ridge could have a higher distribution of α_{vir} values for a few different reasons: the clouds are subjected to an external pressure, the clouds are in freefall, or the clouds are unbounded. The even distribution of the Ridge clouds along the virial line in Figure 11 rather than clustering around a consistent range of pressures makes it seem unlikely that an external pressure has a large influence here. The clouds being

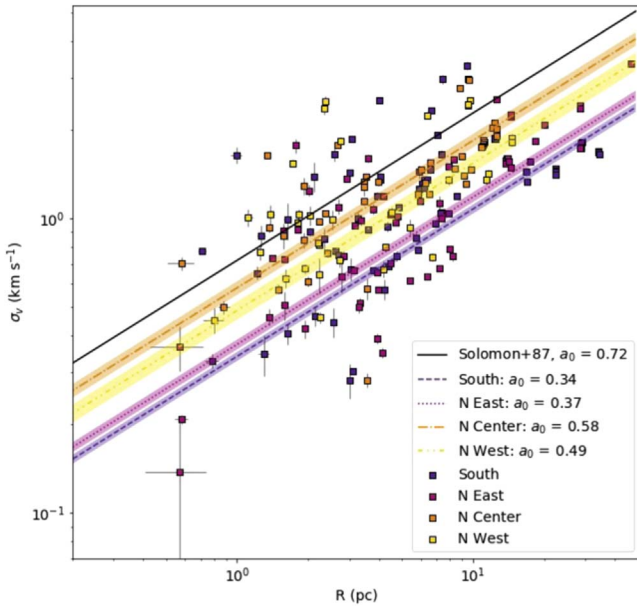


Figure 16. Line widths plotted against sizes of structures in the Ridge, colored by their region within the Ridge. We fit a power law with a fixed slope of $a_1 = 0.5$ to each region’s structures and find that the South and NE regions have the lowest intercepts, indicating low kinetic energy in these regions. The NC region has the highest intercept, indicating that it has the highest kinetic energy.

in freefall collapse could also explain the higher α_{vir} values, but this scenario seems inconsistent with the low kinetic energies indicated in the size–line width plots (Figure 9) and the low amount of star formation. It seems most likely that the clouds in the Ridge tend to be less gravitationally bound than the clouds in the other star-forming regions. This could be due to low gas density, which would make it harder for the clouds to hold together or begin gravitational collapse.

This finding may also have implications for the types of stars and clusters formed based on the density of gas forming those stars. Indebetouw et al. (2008) find that the Ridge is still forming stars but preferentially forms low-mass clusters that do not sample a standard initial mass function (such as Kroupa 2002) well and so do not produce many massive stars. This aligns well with our finding that at this resolution structures in the Ridge have surface densities that fall below the threshold for massive-star formation of $A_V > 8$ mag from Lada et al. (2010). Meanwhile, 30 Dor structures are distributed around that threshold, and the massive-star-forming regions N159 and N113 have average surface densities well above that threshold.

The gradient in star-forming potential from 30 Dor, from N159, and through the Ridge seems consistent with the interaction histories of the LMC and SMC proposed by Besla et al. (2012), in which the SMC collided with the LMC in the past 250 Myr. Recent numerical simulations have further constrained that interaction to the SMC colliding with the LMC 140–160 Myr ago with an impact parameter of ~ 5 kpc (Choi et al. 2022). The Magellanic Bridge connecting the two galaxies is likely the result of such an interaction, and the Molecular Ridge extends from 30 Dor in the direction of the Bridge, suggesting a potential connection between the two structures. The current relative velocities of the LMC and SMC are estimated to be $\sim 100 \text{ km s}^{-1}$ (Zivick et al. 2019), meaning that during such a collision the SMC’s motion through the

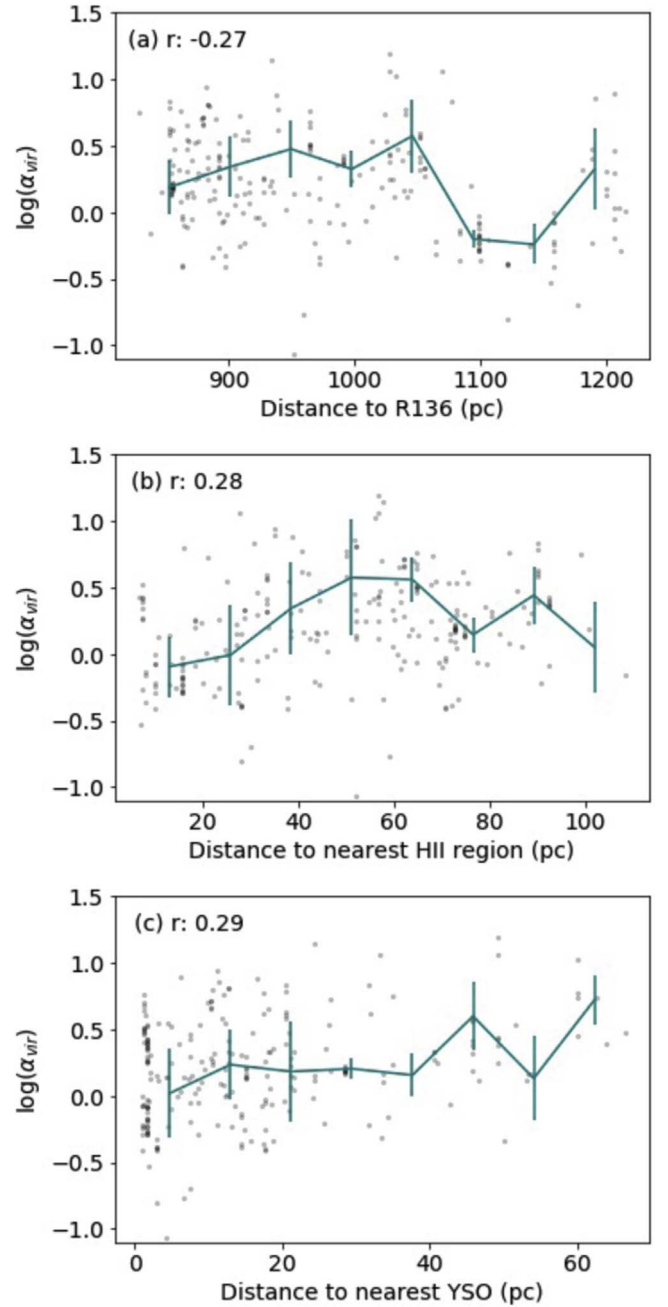


Figure 17. Values of α_{vir} in the Ridge plotted against the structure’s distance to R136 (top), the nearest H II region (middle), and the nearest YSO (bottom). All three show similarly weak correlations based on Pearson’s correlation coefficients, shown in the upper left corner.

LMC would be supersonic for the molecular gas, creating shocks and overdensities in the molecular clouds. The extended Magellanic Streams seen in H I gas are also likely caused in part by close interactions between the LMC and SMC, as well as their interactions with the Milky Way (e.g., Lucchini et al. 2021), although this structure occurs on much larger size scales than the regions studied here.

This interaction scenario is also supported by the findings of Furuta et al. (2019) that the gas in the regions around 30 Dor and N159 has a lower measured $A_V/N(\text{H})$ than the rest of the LMC and is instead consistent with gas in the SMC. Furuta et al. (2021) proposed a geometry in which gas from the SMC

is colliding with the LMC disk moving north to south, forming R136 in 30 Dor and then N159.

The LMC–SMC interaction and subsequent tidal effects would have increased the turbulent motion in the molecular gas, which could have led to the formation of R136 and the older populations in the 30 Dor region (Rahner et al. 2018). To create an SSC like R136 that has a mass of $\sim 10^5 M_\odot$, the initial molecular cloud would have needed to start with a mass of at least $\sim 2 \times 10^5 M_\odot$, assuming a maximum star formation efficiency for SSCs of 50% (Ashman & Zepf 2001; Kroupa et al. 2001; Grudić et al. 2018). Johnson et al. (2015) further required that to form an SSC, the initial molecular cloud must contain this large mass within a maximum radius of 25 pc. None of the molecular cloud structures in 30 Dor meet these criteria, and so they are not capable of creating an SSC like R136, suggesting that the gas conditions during the peak of star formation in 30 Dor were much more extreme than they currently are. The molecular cloud that created R136 more likely appeared similar in physical conditions to the potential SSC precursor cloud observed in the merging Antennae galaxies (Johnson et al. 2015). Finn et al. (2019) observed that this cloud has a large α_{vir} parameter and would require high external pressure in order to remain bound. They also found evidence that this pressure is supplied by cloud–cloud collision. Fukui et al. (2017) presented evidence that R136 was also created by a tidally induced collision of large-scale H I clouds, which would align with the idea that the molecular cloud precursor to R136 was subject to high external pressure from a galactic interaction.

Fukui et al. (2015) also found evidence for a cloud–cloud collision triggering the formation of high-mass YSOs in N159, and follow-up work by Fukui et al. (2019) and Tokuda et al. (2019) suggests that this collision is associated with the same large-scale colliding flows that triggered the formation of R136 cited above. N159 is currently forming more massive-star clusters than the 30 Dor region and hosts a massive molecular core of $\sim 10^4 M_\odot$ within a ~ 1 pc radius (Tokuda et al. 2022), but it does not have any molecular cloud structures measured in this analysis that meet the SSC-forming criteria cited above (a mass of at least $2 \times 10^5 M_\odot$ within a radius of 25 pc; Johnson et al. 2015). This ongoing star formation in N159 is consistent with our finding that the structures are currently near or below virial equilibrium and so are likely to collapse and form stars, but they do not show signs of requiring a high external pressure to be bound as seen in SSC-forming clouds.

If 30 Dor and N159 experienced cloud collisions induced by the interaction of the SMC and LMC, it would be reasonable to expect that as the SMC moved away from the LMC, the gas conditions became less extreme (and so N159 is not forming stars as intensely as 30 Dor once was) and some molecular gas may also have been pulled out of the SMC in the direction of the Magellanic Bridge, meaning that the Ridge may even be a denser extension of the Magellanic Bridge. The Ridge could be this gas, and our finding that it is less dense than the gas in 30 Dor and N159 is consistent with that interpretation. It is also consistent with our finding that the northern regions have higher kinetic energy and densities and so are more similar to 30 Dor and N159 than the molecular gas toward the south of the Ridge.

This proposed scenario demonstrates how galaxy interactions can create regions that both over- and underproduce stars when compared to often-applied scaling relations. This effect

can be important when accounting for star formation in galaxy simulations, especially given the importance of dwarf galaxy mergers in the evolution of galaxies over cosmic time. It would be interesting to see whether any simulations of dwarf galaxy interactions, especially of the SMC–LMC interaction specifically, are able to recreate the morphology of the Ridge and the gas conditions that we see along its extent. Such simulations may also help clarify the timescales of the interaction between the galaxies and the subsequent tidal effects that may lead to further cloud collisions and the eventual onset of star formation in regions like 30 Dor.

10. Conclusions

We present a comparison of ^{13}CO observations of the Molecular Ridge, 30 Dor, N159, and N113 in the LMC. The last three regions are all actively forming massive stars, while the Ridge is not, despite its large reservoir of molecular gas. We use dendrograms and clump-finding algorithms to segment the emission and analyze the physical conditions of those structures. Our major findings are summarized below.

1. The Ridge, 30 Dor, and N113 have fractal dimensions of $D_2 = 1.50 \pm 0.02$, 1.44 ± 0.02 , and 1.42 ± 0.07 , respectively. These are similar enough that it seems unlikely that the difference in star formation activity between the regions is related to a difference in cloud morphology and hierarchical structure. These values are also consistent with other measurements of the fractal dimension within the LMC, SMC, and Milky Way (Section 3.3).
2. Comparing size–line width relations in the Ridge, 30 Dor, N159, and N113 indicates that the Ridge has significantly lower kinetic energy at given size scales when compared to the massive-star-forming regions. This would rule out the possibility that the Ridge has lower rates of massive-star formation because it is supported against collapse due to excess kinetic energy (Section 5).
3. The Ridge has higher values of α_{vir} than 30 Dor, although the absolute scaling of these values relative to virial equilibrium is unclear owing to large uncertainties in the mass estimate. This appears to be driven by significantly lower surface densities in the Ridge, since we know from the size–line width relations that the Ridge also has lower kinetic energy than 30 Dor. We find as well that the structures in the Ridge fall below the Lada et al. (2010) threshold of $A_V > 8$ mag for massive-star formation, while 30 Dor structures are distributed around this threshold and the average surface densities in N159 and N113 are well above this threshold. These results suggest that the Ridge has lower rates of massive-star formation because it has significantly less dense gas than 30 Dor, although from Finn et al. (2021) we know that the surface density of the gas does not necessarily trace the non-LTE-fitted volume density of the gas (Section 6).
4. Within the Ridge, there is some variation in physical properties. The region in the northeast has a significantly lower α_{vir} distribution than the other regions, likely partially driven by having a low specific kinetic energy and relatively high densities (Section 7).
5. The α_{vir} values measured for structures are only weakly correlated with distance from the super star cluster R136 in 30 Dor, suggesting that such star clusters do not affect gas properties at kiloparsec distances. The α_{vir} values

similarly show only a weak correlation with the distances to the nearest YSO and the nearest H II region, suggesting that local star formation has a minimal influence on gas conditions or that the YSOs are slightly more likely to be spatially coincident with gas that has the right conditions for further star formation (Section 8).

This research is supported by NSF grants 1413231 and 1716335 (PI: K. Johnson), NSF grant 2009624, and NSF AAG award AST 1312902 to the University of Virginia (PI: R. Indebetouw). This material is based on work supported by the National Science Foundation Graduate Research Fellowship Program under grant No. 1842490. Any opinions, findings, and conclusions or recommendations expressed in this material are those of the author(s) and do not necessarily reflect the views of the National Science Foundation. T.W. acknowledges support from NSF AAG award 2009849. The material is based on work supported by NASA under award No. 80GSFC21M0002 (M.S.). K.T. acknowledges support from NAOJ ALMA Scientific Research grant Nos. 2022-22B and Grants-in-Aid for Scientific Research (KAKENHI) of Japan Society for the Promotion of Science (JSPS; grant Nos. JP21H00049 and JP21K13962).












This paper makes use of the following ALMA data: ADS/JAO.ALMA#2012.1.00554.S, ADS/JAO.ALMA#2015.1.00196.S, ADS/JAO.ALMA#2015.1.01388.S, ADS/JAO.ALMA#2017.1.00271.S, ADS/JAO.ALMA#2019.1.00843. ALMA is a partnership of ESO (representing its member states), NSF (USA) and NINS (Japan), together with NRC (Canada), NSC and ASIAA (Taiwan), and KASI (Republic of Korea), in cooperation with the Republic of Chile. The Joint ALMA Observatory is operated by ESO, AUI/NRAO and NAOJ. The National Radio Astronomy Observatory is a facility of the National Science Foundation operated under cooperative agreement by Associated Universities, Inc.

Based on observations with the Atacama Pathfinder EXperiment (APEX) telescope. APEX is a collaboration between the Max Planck Institute for Radio Astronomy, the European Southern Observatory, and the Onsala Space Observatory. Swedish observations on APEX are supported through Swedish Research Council grant No 2017-00648.

Facility: ALMA.

Software: Pipeline-CASA51-P2-B v.40896 (L. Davis 2021, in preparation), CASA (v.5.1.1-5, v.5.6.1; McMullin et al. 2007), *astrodendro* (Rosolowsky et al. 2008), *quickclump* (Sidorin 2017), *Astropy* (Astropy Collaboration et al. 2013), *Matplotlib* (Hunter 2007), *NumPy* (Harris et al. 2020), *SciPy* (Virtanen et al. 2020).

ORCID iDs

Molly K. Finn  <https://orcid.org/0000-0001-9338-2594>
 Remy Indebetouw  <https://orcid.org/0000-0002-4663-6827>
 Kelsey E. Johnson  <https://orcid.org/0000-0001-8348-2671>
 Allison H. Costa  <https://orcid.org/0000-0002-7408-7589>
 C.-H. Rosie Chen  <https://orcid.org/0000-0002-3925-9365>
 Akiko Kawamura  <https://orcid.org/0000-0001-7813-0380>
 Toshikazu Onishi  <https://orcid.org/0000-0001-7826-3837>
 Jürgen Ott  <https://orcid.org/0000-0001-8224-1956>
 Marta Sewiło  <https://orcid.org/0000-0003-2248-6032>
 Kazuki Tokuda  <https://orcid.org/0000-0002-2062-1600>
 Tony Wong  <https://orcid.org/0000-0002-7759-0585>

Sarolta Zahorecz  <https://orcid.org/0000-0001-6149-1278>

References

- Ashman, K. M., & Zepf, S. E. 2001, *AJ*, **122**, 1888
 Astropy Collaboration, Robitaille, T. P., Tollerud, E. J., et al. 2013, *A&A*, **558**, A33
 Besla, G., Kallivayalil, N., Hernquist, L., et al. 2012, *MNRAS*, **421**, 2109
 Bica, E., Claria, J. J., Dottori, H., Santos, J. F. C. J., & Piatti, A. E. 1996, *ApJS*, **102**, 57
 Bolatto, A. D., Wolfire, M., & Leroy, A. K. 2013, *ARA&A*, **51**, 207
 Calzetti, D., Kennicutt, R. C., Engelbracht, C. W., et al. 2007, *ApJ*, **666**, 870
 Chen, C. H. R., Indebetouw, R., Chu, Y.-H., et al. 2010, *ApJ*, **721**, 1206
 Chevance, M., Madden, S. C., Fischer, C., et al. 2020, *MNRAS*, **494**, 5279
 Choi, Y., Olsen, K. A. G., Besla, G., et al. 2022, *ApJ*, **927**, 153
 Cignoni, M., Sabbi, E., van der Marel, R. P., et al. 2015, *ApJ*, **811**, 76
 Cohen, R. S., Dame, T. M., Garay, G., et al. 1988, *ApJL*, **331**, L95
 Davies, R. D., Elliott, K. H., & Meaburn, J. 1976, *MmRAS*, **81**, 89
 Dobashi, K., Bernard, J. P., Hughes, A., et al. 2008, *A&A*, **484**, 205
 Elmegreen, B. G., & Falgarone, E. 1996, *ApJ*, **471**, 816
 Elmegreen, B. G., Kim, S., & Staveley-Smith, L. 2001, *ApJ*, **548**, 749
 Falgarone, E., Phillips, T. G., & Walker, C. K. 1991, *ApJ*, **378**, 186
 Field, G. B., Blackman, E. G., & Keto, E. R. 2011, *MNRAS*, **416**, 710
 Finn, M. K., Indebetouw, R., Johnson, K. E., et al. 2021, *ApJ*, **917**, 106
 Finn, M. K., Johnson, K. E., Brogan, C. L., et al. 2019, *ApJ*, **874**, 120
 Fomalont, E., van Kempen, T., Kneissl, R., et al. 2014, *Msngr*, **155**, 19
 Fukui, Y., Harada, R., Tokuda, K., et al. 2015, *ApJL*, **807**, L4
 Fukui, Y., Kawamura, A., Minamidani, T., et al. 2008, *ApJS*, **178**, 56
 Fukui, Y., Tokuda, K., Saigo, K., et al. 2019, *ApJ*, **886**, 14
 Fukui, Y., Tsuge, K., Sano, H., et al. 2017, *PASJ*, **69**, L5
 Furuta, T., Kaneda, H., Kokusho, T., et al. 2019, *PASJ*, **71**, 95
 Furuta, T., Kaneda, H., Kokusho, T., et al. 2021, *PASJ*, **73**, 864
 Goodman, A. A., Barranco, J. A., Wilner, D. J., & Heyer, M. H. 1998, *ApJ*, **504**, 223
 Grudić, M. Y., Hopkins, P. F., Faucher-Giguère, C.-A., et al. 2018, *MNRAS*, **475**, 3511
 Gruendl, R. A., & Chu, Y.-H. 2009, *ApJS*, **184**, 172
 Harris, C. R., Millman, K. J., van der Walt, S. J., et al. 2020, *Natur*, **585**, 357
 Henize, K. G. 1956, *ApJS*, **2**, 315
 Hunter, J. D. 2007, *CSE*, **9**, 90
 Indebetouw, R., Whitney, B. A., Kawamura, A., et al. 2008, *AJ*, **136**, 1442
 Indebetouw, R., Wong, T., Chen, C. H. R., et al. 2020, *ApJ*, **888**, 56
 Johnson, K. E., Leroy, A. K., Indebetouw, R., et al. 2015, *ApJ*, **806**, 35
 Kennicutt, R. C. J. 1998, *ApJ*, **498**, 541
 Kroupa, P. 2002, *Sci*, **295**, 82
 Kroupa, P., Aarseth, S., & Hurley, J. 2001, *MNRAS*, **321**, 699
 Lada, C. J., Lombardi, M., & Alves, J. F. 2010, *ApJ*, **724**, 687
 Larson, R. B. 1981, *MNRAS*, **194**, 809
 Longmore, S. N., Bally, J., Testi, L., et al. 2013, *MNRAS*, **429**, 987
 Lucchini, S., D’Onghia, E., & Fox, A. J. 2021, *ApJL*, **921**, L36
 McMullin, J. P., Waters, B., Schiebel, D., Young, W., & Golap, K. 2007, in ASP Conf. Ser. 356, *Astronomical Data Analysis Software and Systems XVI*, ed. R. A. Shaw, F. Hill, & D. J. Bell (San Francisco, CA: ASP), **127**
 Meixner, M., Gordon, K. D., Indebetouw, R., et al. 2006, *AJ*, **132**, 2268
 Meixner, M., Panuzzo, P., Roman-Duval, J., et al. 2013, *AJ*, **146**, 62
 Miller, A. E., Cioni, M.-R. L., de Grijs, R., et al. 2022, *MNRAS*, **512**, 1196
 Mizuno, N., Yamaguchi, R., Mizuno, A., et al. 2001, *PASJ*, **53**, 971
 Nayak, O., Meixner, M., Fukui, Y., et al. 2018, *ApJ*, **854**, 154
 Nayak, O., Meixner, M., Indebetouw, R., et al. 2016, *ApJ*, **831**, 32
 O’Neill, T. J., Indebetouw, R., Bolatto, A. D., Madden, S. C., & Wong, T. 2022, *arXiv:2205.13533*
 Oka, T., Hasegawa, T., Sato, F., et al. 2001, *ApJ*, **562**, 348
 Pietrzyński, G., Graczyk, D., Gieren, W., et al. 2013, *Natur*, **495**, 76
 Rahner, D., Pellegrini, E. W., Glover, S. C. O., & Klessen, R. S. 2018, *MNRAS*, **473**, L11
 Rolleston, W. R. J., Trundle, C., & Dufton, P. L. 2002, *A&A*, **396**, 53
 Rosolowsky, E. W., Pineda, J. E., Kauffmann, J., & Goodman, A. A. 2008, *ApJ*, **679**, 1338
 Sabbi, E., Lennon, D. J., Anderson, J., et al. 2016, *ApJS*, **222**, 11
 Sánchez, N., Alfaro, E. J., & Pérez, E. 2007, *ApJ*, **656**, 222
 Seale, J. P., Looney, L. W., Wong, T., et al. 2012, *ApJ*, **751**, 42
 Seale, J. P., Meixner, M., Sewiło, M., et al. 2014, *AJ*, **148**, 124
 Sewiło, M., Indebetouw, R., Carlson, L. R., et al. 2010, *A&A*, **518**, L73
 Sidorin, V. 2017, *Quickclump: Identify clumps within a 3D FITS datacube*, *Astrophysics Source Code Library*, ascl:1704.006
 Solomon, P. M., Rivolo, A. R., Barrett, J., & Yahil, A. 1987, *ApJ*, **319**, 730

- Sorai, K., Hasegawa, T., Booth, R. S., et al. 2001, [ApJ](#), **551**, 794
- Sun, N.-C., de Grijs, R., Cioni, M.-R. L., et al. 2018, [ApJ](#), **858**, 31
- Tokuda, K., Fukui, Y., Harada, R., et al. 2019, [ApJ](#), **886**, 15
- Tokuda, K., Minami, T., Fukui, Y., et al. 2022, [ApJ](#), **933**, 20
- van der Marel, R. P., & Kallivayalil, N. 2014, [ApJ](#), **781**, 121
- Virtanen, P., Gommers, R., Oliphant, T. E., et al. 2020, [Nature Methods](#), **17**, 261
- Walborn, N. R., Barbá, R. H., & Sewilo, M. M. 2013, [AJ](#), **145**, 98
- Ward, J. L., Oliveira, J. M., van Loon, J. T., & Sewilo, M. 2016, [MNRAS](#), **455**, 2345
- Whitney, B. A., Sewilo, M., Indebetouw, R., et al. 2008, [AJ](#), **136**, 18
- Wong, T., Hughes, A., Tokuda, K., et al. 2019, [ApJ](#), **885**, 50
- Wong, T., Oudshoorn, L., Sofovich, E., et al. 2022, [ApJ](#), **932**, 47
- Yamaguchi, R., Mizuno, N., Mizuno, A., et al. 2001, [PASJ](#), **53**, 985
- Zivick, P., Kallivayalil, N., Besla, G., et al. 2019, [ApJ](#), **874**, 78